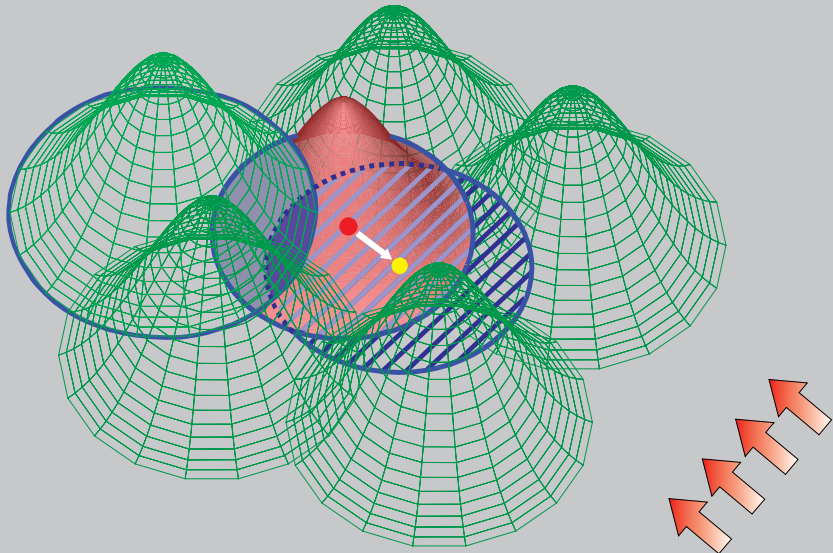


Reprinted from

CMES

Computer Modeling in Engineering & Sciences

Founder and Editor-in-Chief:
Satya N. Atluri



ISSN: 1526-1492 (print)
ISSN: 1526-1506 (on-line)

Tech Science Press

Numerical Investigation on Dynamical Response of Aluminum Foam Subject to Hypervelocity Impact With Material Point Method

Weiwei Gong¹, Yan Liu¹, Xiong Zhang^{1,2}, Honglei Ma³

Abstract: Owing to its low density and good energy absorption capability, aluminum foam is an excellent protective material for spacecraft against debris impact. However, because of its complicated microstructure, it is very difficult to generate a FEM mesh accounting for the real microstructure of the alluminum foam. On the contrary, it is very easy to model three-dimensional problems with very complicated geometry with meshfree/meshless methods. Furthermore, the material point method has obvious advantages in modeling problems involving extreme large deformation problems like hypervelocity impact problem. In this paper, a three-dimensional material point model accounting for the real microstructure of aluminum foam is created based on the scanned CT images, and is used to study the protective capacity of aluminum foam in different Whipple shield structures using our three-dimensional material point method code, MPM3D. The simulation results agree well with the experimental data.

Keywords: whipple shield structure, aluminum foam, debris impact, material point method, hypervelocity impact

1 Introduction

Compared with the solid metals, the metal foam has a lower density. Compared with the thin-walled tube and composite laminate, the metal foam tends to be more isotropic with a long stage of the plateau stress. Compared with the polymer foam, the metal foam has a higher stress plateau. Thus the metal foam has good energy absorption characteristics. In recent years, the metal foam has been receiving much attention [Ashby, Evans, Fleck, Gibson, Hutchinson, and Wadley (2006); Degischer and Kriszt (2005); Baumeister, Banhart, and Weber (1997); Hu, Liu, Wang, and

¹ School of Aerospace, Tsinghua University, Beijing 100084, P. R. China.

² Corresponding author: xzhang@tsinghua.edu.cn.

³ China Astronaut Research and Training Center, Beijing 100094, P. R. China

Song (1999); Grenested and Bassinet (2000)].

A large number of studies show that the stress-strain response of aluminum foam has three typical stages under compression [Degischer and Kriszt (2005); Gibson and Ashby (1997); Bart-Smith, Bastawros, Mumm, Evans, Syneck, and Wadley (1998); Gama, Bogetti, Fink, Yu, Claar, Eifert, and Gillespie. (2001)]: elastic deformation stage, plastic platform stage, and compact stage. Under compression, the porous material firstly generates the elastic deformation and the pore walls are bent. Within each band several pore walls experience plastic buckling and bending but others remain elastic. And then plastic deformation occurs, the internal cavities of material begin collapsing due to elastic bending, plastic buckling and creep. As the deformation continues, the material enters the compact stage and the internal cavities are almost completely collapsed. Then the neighboring walls contact and the solid material is compressed. In this stage, the density of metal foam is increasingly close to its base metal and the strength is also enhanced. Because the metal foam has such a unique compression behavior, it is easy to deform under the external impact load. The metal foam consumes a lot of energy during compressing because of its large deformation under the plat stress, the energy is dissipated through the deformation, collapse and rupture of the cell pores inside the metal foam. Hence, the metal foam can effectively absorb the impact energy from the outside [Gibson and Ashby (1997)]. The dynamic behaviors of metal foam are decided by the mechanical properties of the base material as well as the microstructure of the foam.

The most widely-used constitutive models of the aluminum foam are continuous models. Gibson, Ashby, Zhang, and Triantafillou (1989) brought forward the first yield surface equation of the foam materials. Chen and Lu (2000) obtained the strain potential function of foam materials based on the assumption that the yield stress remains the same during stretching or compressing. These two models are isotropic ones and do not consider the different mechanical properties under tension and compression. Deshpande and Fleck (2000) proposed an isotropic constitutive model based on the uniaxial compression test. This model can well describe the mechanical behaviors of aluminum foam under compression, but it does not consider the anisotropic characteristics caused by stretching and the randomly distributed internal cavities. Crushable foam model (material model No. 63 in LS-DYNA) defines the yield surface in the principal stress space [Hallquist (2006)]. Bilkhu and Dubois established the constitutive model of foam materials based on the experiments of uniaxial and triaxial compressive tests [Hallquist (2006)]. These two models consider the difference between stretching and compressing, but ignore the randomly distributed internal cavities. Schreyer model is an anisotropic hardening model considering the anisotropic characteristics of the metal foam, but can not reveal the discontinuous characteristic caused by the internal cavities [Schreyer, Zuo,

and Maji (1994)]. It can be seen from the above discussion that it is very difficult to give an ideal theoretical model for the metal foam. In addition, in the hypervelocity impact problems, when the projectile collides with the target (the typical velocity is several kilometers per second), it fragments into many small particles forming the debris cloud. The particles hit the cell walls and cause fragmentation and phase transitions on the mesoscopic scale [Ma, Jia, and Pang (2007)]. Therefore, it is desirable to establish the micro geometry model of the metal foam. Thus the base material model which has been fully studied can be used for the metal foam. In this way, the mechanical behaviors of the metal foam can be described more accurately.

The microstructure of the metal foam is very complicated. A large number of randomly distributed cavities exist inside the foam, and sometimes both open-cell and closed-cell exist at the same time, which is a big challenge for finite element modeling. Researchers have proposed some microstructure models for the aluminum foam [Gibson and Ashby (1997); Czekanski, Attia, Meguid, and Elbestawi (2005); Ma, Jia, and Pang (2007)], such as two-dimensional periodic hexagonal honeycomb model. But these models can only be used to in some limited cases. A periodic three-dimensional microscopic model is produced in a multi-polyhedron space, which is mostly based on tetrakaidecahedron [Gibson and Ashby (1997); Demiray, Becker, and Hohe (2007)]. These models can not fully exhibit the real microstructure of metal foams. Under hypervelocity impact, the projectile fragments into many small particles after impacting the metal foam, which hit the cell walls and cause fragmentation and phase transitions on the microscale. Therefore, the real microstructure is needed in such station.

Recently, the meshfree methods have been developed and widely used in mechanics [Gu and Liu (2001); Gu and Zhang (2008); Gan, Chen, and Montgomery-Smith (2011); Rabczuk and Eibl (2006); Li and Liu (2002); Liu and Liu (2005)]. The meshfree method can avoid the mesh distortion because it uses the discrete points to construct trial functions. The material point method (MPM), as one of the highly effective meshfree method proposed by Sulsky, Chen, and Schreyer (1994), is an extension of the particle-in-cell method (PIC) [Brackbill, Kothe, and Ruppel (1988)] in computational fluid mechanics to solid mechanics, which combines the advantages of both Lagrangian method and Eulerian method. In MPM, material domain is discretized by a set of material points (particles) that carry all state variables. The motion of these particles represents the motion and deformation of material. A background grid is used to solve the momentum equations and calculate spatial derivatives. Incorporation of constitutive models in MPM is relatively straightforward. In each time step, particles deform together with the grid nodes, so MPM avoids the difficulties associated with convection terms between adjacent elements. In the next time step, the deformed grid is discarded and a new regular grid is used

to avoid mesh distortion [Ma, Zhang, and Qiu (2009)]. Owing to these characteristics, MPM has obvious advantages in modeling problems involving extreme large deformation, such as impact, contact, material damage and solid-fluid coupling problems.

Although many excellent automatic mesh generators are available, it is still very difficult to create a finite element model for the complicated and irregular geometry. MPM discretizes a material domain by a set of particles rather than finite element mesh, so it is very easy to model three-dimensional problems with very complicated geometry like the metal foam with MPM. In this paper, a three-dimensional MPM model accounting for the real microstructure of aluminum foam is proposed based on the micro-CT scanned images, and is used to study the dynamical behavior of the filling and the sandwich Whipple shield structures subject to debris impact by using the three-dimensional material point method code MPM3D developed by the Computational Dynamics Laboratory at Tsinghua University [Ma, Zhang, Lian, and Zhou (2009); Ma, Zhang, and Huang (2010); Zhang, Zhang, and Liu (2010)].

2 Brief Introduction to Material Point Method

The material point method uses a set of uniform background grid fixed in the space and a group of particles (called the material points) moving over the background grid at the same time. In each time step, the the particles are rigidly attached to background grid to generate the following discrete equations of motion,

$$\dot{p}_{il} = f_{il}^{int} + f_{il}^{ext}, \quad I = 1, 2, \dots, n_g \tag{1}$$

which will be solved on the background grid nodes. In Eq.(1)

$$p_{il} = m_I v_{il} \tag{2}$$

is the momentum of grid node I ,

$$f_{il}^{int} = - \sum_{p=1}^{n_p} N_{Ip,j} \sigma_{ijp} \frac{m_p}{\rho_p} \tag{3}$$

is the internal nodal force, and

$$f_{il}^{ext} = \sum_{p=1}^{n_p} m_p N_{Ip} f_{ip} + \sum_{p=1}^{n_p} N_{Ip} \bar{t}_{ip} h^{-1} \frac{m_p}{\rho_p} \tag{4}$$

is the external force. The subscript i is the spacial index. n_g is the total number of grid nodes, and n_p is the number of particles in the cell linked with grid node I . m_I is the mass of the grid point I , v_i is the velocity component, σ_{ij} is the stress

component, and ρ is the density. The subscript I and p denote that the associated variables belong to the grid node I and the particle p , respectively. f_{ip} and \bar{t}_{ip} are the body force per unit mass and the prescribed traction exerted on the particle p , respectively.

The discrete equations of motion (1) come from the weakform of the updated Lagrange description and the standard finite element approximation spanned by the shape functions constructed on the grid nodes

$$w_p = \sum_{I=1}^{n_g} N_{Ip} w_I \tag{5}$$

where w is a field function. If the eight-point hexahedron cell is used, the shape function of node I can be given by

$$N_I = \frac{1}{8}(1 + \xi \xi_I)(1 + \eta \eta_I)(1 + \zeta \zeta_I), I = 1, 2, \dots, 8 \tag{6}$$

where ξ, η, ζ are the natural coordinates which take values of ± 1 at the grid nodes. The abbreviation $N_{Ip} = N_I(x_p)$ has been used in the above equations for simplicity. The construction of equations of motion is actually a mapping process from the particles to the grid nodes. The momenta, the masses and the forces of the particles are mapped to the grid nodes to form the nodal mass, the nodal internal and external forces.

If all the particles variables at time level t^k are known, they are mapped to the grid nodes to construct the equations of motion at the beginning of each time step. After Eq.(1) is solved, the accelerations and the velocities of the grid nodes are obtained, which will be mapped back to the particles for the purpose of updating the velocities and the positions of the particles. Then the constitutive models are invoked to update the stresses of the particles from the stresses at time level t^k and the strain increment. Three kinds of stress update algorithms, USF, USL, and MUSL, have been widely used in MPM[Bardenhagen (2002)]. The MUSL algorithm is adopted in this paper for its stability and energy conservation properties. In MUSL algorithm, the updated particle momentum is mapped back to the computational grid again at the end of each time step to calculate the nodal velocity

$$v_{iI}^{k+\frac{1}{2}} = \sum_{p=1}^{n_p} p_{ip}^{k+\frac{1}{2}} N_{Ip}^k / m_I^k \tag{7}$$

for the incremental strain and then update the stress. The last step in each time step is to abandon the deformed background grid and use the same undeformed grid for the beginning of next time step.

Equations of motion of material point method are very similar to those of finite element method, but it should be noted that the two methods are really different in each time step. The Lagrangian finite element method employs Lagrangian descriptions for both the nodes and the quadrature points. In MPM, however, the particles carry all the physical information and are described in Lagrangian way, and the background grid is only used to construct and solve equations of motion and they are fixed in the space. So MPM does not rely on the mesh, and there is no mesh distortion or entanglement problem.

The lumped mass matrix is used for efficient explicit integration in time domain. The central difference algorithm has been adopted in our computation. The critical time step size Δt_{cr} is determined by

$$\Delta t_{cr} = \min_e \frac{l_e}{c + |u|} \quad (8)$$

where l_e is the characteristic length of the cell e , u is the particle velocity, and c is the isentropic sound speed.

In MPM, Spurious oscillation may occur as particles cross the boundaries of the background grid during the solution process, which is called the cell-crossing noise and caused by using the linear shaped function whose derivatives are discontinuous across the background grid boundaries. To resolve this problem, a generalization of MPM named generalized interpolation material point (GIMP) method has been proposed by Bardenhagen and Kober [Bardenhagen and Kober (2000); Ma, Zhang, and Qiu (2009)] using a variational form and incorporating a Petrov-Galerkin discretization scheme. The numerical noise can be minimized by using a C^1 continuous shape functions. GIMP has been successfully applied in nanoindentation [Ma, Lu, Wang, Roy, Hornung, Wissink, and Komanduri (2005)], crack propagation problems [Ma, Lu, Wang, Hornung, Wissink, and Komanduri (2006)], open-cell foam densification problems [Carlo, Xiao, and Tieman (2006)], and closed-cell polymer foam compression problems [Daphalapurkar, Hanan, Phelps, Bale, and Lu (2008)]. GIMP has also been adopted to improve the accuracy and suppress the numerical noise.

As has been focused in these years, MPM theory is developing fast. The adaptive algorithm [Ma, Zhang, Lian, and Zhou (2009)], the contact algorithms [Ma, Zhang, and Huang (2010)], coupling with the finite element method [Lian, Zhang, and Liu (2011)], and the parallelization [Zhang, Zhang, and Liu (2010)] for MPM have been proposed recently. The readers can refer to the above references for detailed formulae and implementation of material point method.

3 Material point modeling of the microstructure of aluminum foam

Owing to the particle characteristics, it is appropriate to use MPM to model three-dimensional problems with very complicated geometry such as the metal foam. The technique to establish a three-dimensional MPM model accounting for the real microstructure of aluminum foam based on the micro-CT scanned images is developed. The reconstructed MPM model can be further used to investigate the mechanical, thermal and other properties of the Whipple shield structure. The micro CT is specially designed for detecting the internal three-dimensional structure and material characteristics. Using the thin-section tomography, three-dimensional high-resolution images of the material can be reconstructed, based on which we can study the influences of the microstructure of the samples (such as anisotropic characteristics and heterogeneity of density) on the macroscopic properties. In the experiment, the scanned CT images of the sample are gained by the GE Explore Locus SP micro-CT scanner. with scanning resolution of $14 \mu\text{m}$. During each scanning step, X-rays bathed the aluminum foam sample with an initial intensity I_0 . The foam sample absorbed a part of the X-ray energy and the initial intensity was thus attenuated to I , which was detected by X-ray detector from different angles and different positions. Measurement of all rays was expressed as the sum of the attenuation values in pixels through which each ray had passed [Goldman (2007)]. It was convenient to use CT number to replace the attenuation value as

$$CT = \frac{\mu_m - \mu_{\text{water}}}{\mu_{\text{water}}} * 1000 \quad (9)$$

where μ_m and μ_{water} were the absorption coefficients of the material and the water. The CT numbers of material were calculated based on the detected X-ray intensities at all positions and angles, then saved as .dicom file, which contained all the information of the microstructure and volume density distribution of the scanned aluminum foam.

To reconstruct the three-dimensional MPM aluminum foam model, the gray intensity, sample size and distance between neighboring pixels were extracted from the CT number files. Matlab software provides us a perfect mathematical tool to analyze the scanned images of aluminum foam samples. It was obvious that the metal absorbed more energy than air, thus the gray intensities at pixels where aluminum existed were much smaller than those of air. Judging by the intensities of pixels, we could separate the pixels of aluminum from the pixels of air in the holes. Furthermore, the density distribution of aluminum foam could be determined by analyzing the gray intensity distribution. Once the density distribution was decided, the coordinate values of material particles could be calculated according to the pixel distance, location and sample size. Although the MPM method has high

efficiency, it was indeed unrealistic to include all the material particles in the computation because of the great amount. We had to combine the neighboring pixels into one without changing the sample shape. To merge the pixels efficiently, we defined a regular three-dimensional background grid which covered all the pixels, then searched for the total number and locations of pixels located in each cell. After that, all the pixels in each cell were merged into one particle located at their centroid, and its mass is calculated as the mass per pixel, which equals the total mass of the sample divided by the total number of pixels, multiplied by the total number of pixels in the cell. Figure 1 shows a typical three-dimensional MPM model of the aluminum foam sample reconstructed from the CT scanned images.



Figure 1: Three-dimensional material point model of aluminum foam

4 material model

The Johnson-Cook plastic model and Mie-Grüneisen equation of state are used in this paper to model the dynamic behavior of the aluminum. The yield stress is expressed as

$$\sigma_y = (A + B(\epsilon^p)^n)(1 + C \ln \dot{\epsilon}^*)(1 - T^{*m}) \quad (10)$$

where $\dot{\epsilon}^* = \dot{\epsilon}^p / \dot{\epsilon}_0$ is the dimensionless equivalent plastic strain rate with $\dot{\epsilon}_0 = 1 \text{ s}^{-1}$, $\dot{\epsilon}^p$ is the plastic strain rate, and A , B , n , C , and m are the material constants which can be obtained from the experiments. The Mie-Grüneisen equation of state can well describe the thermodynamic behaviors of many kinds of solid metals under impact loading, which can be given as

$$p = p_H + \frac{\gamma}{v}(e - e_H) \quad (11)$$

where p_H and e_H are the pressure and internal energy per unit of mass in the Hugoniot curve. γ is a constant defined by

$$\gamma = \frac{3\alpha v}{C_v K} \quad (12)$$

where $3\alpha = (1/v)(\partial v/\partial T)_p$ is the volume thermal expansion coefficient, $K = -(1/v)(\partial v/\partial P)_T$ is the isothermal compression coefficient. $C_v = (\partial e/\partial T)_v$ is the isovolemic specific heat. γ satisfy the equation

$$\frac{\gamma}{v} = \frac{\gamma_0}{v_0} = \text{constant} \tag{13}$$

where γ_0 and v_0 are the Grüneisen constant and the specific volume at zero pressure condition. The Grüneisen constant γ_0 and the linear coefficient s approximately satisfy

$$\gamma_0 \approx 2s - 1 \tag{14}$$

where $s = \frac{u_s - c_0}{u_p}$, u_s is the shock wave speed and u_p is the particle velocity.

5 Numerical examples

A large number of study have been carried out for protection structure of spacecraft under the hypervelocity impact of debris. Whipple (1947) developed a protection structure, now known as the Whipple shield structure, which places a shield outside the spacecraft wall for protection against penetrations by space debris impact. Since 1980s, many different protection shields have been developed based on the Whipple shield structure for different purposes, such as the ripple Whipple shield structure [Schonberg (1990)], stiffened ribs Whipple shield structure [Maclay (1993)], multi-layered impact protection structure [Cour-Palais and Crew (1990); Olsen and Nolen (1993); Shiraki and Terada (1997)], double-bumper shield protection structure [Christiansen and Kerr (1993)], filling Whipple shield structure [Christiansen, Crew, and Kerr (1996)]. European Space Agency studied the aluminum foam protection structure experimentally in the “Enhanced space debris protection project”, and proved that the aluminum foam is one of the best materials for spacecraft protection.

In this section, the three-dimensional micro structure model of aluminum foam created in section 3 is used to study the dynamic behavior of the filling and sandwich Whipple shield structures [Ma (2008); Ma, Jia, and Pang (2007)] subject to debris impact using our MPM3D code. The relative density of the aluminum foam is 27%. The Johnson-Cook plasticity model and Mie-Grüneisen equation of state with material parameters are listed in Tables 1 and 2 [Beissel, Gerlach, and Johnson (2006); Hayhurst and Livingstone (1998)].

5.1 Filling Whipple shield structure

The filling Whipple shield structure subject to the hypervelocity impact is first studied. The schematic diagram of configuration of the filling Whipple shield structure

Table 1: Parameters of Johnson-Cook model[Walsh, Rice, McQueen, and Yarger (1957); Johnson and Cook (1983); Lin, Lin, and Zhao (2006); Ma (2008)]

| Material | G (GPa) | A (MPa) | B (MPa) | C | m | n | T_{room} (K) | T_{melt} (K) |
|----------|-----------|-----------|-----------|-------|-----|------|----------------|----------------|
| Al2024 | 27.6 | 265 | 426 | 0.015 | 1.0 | 0.34 | 300 | 775 |
| 2A12 | 26 | 265 | 426 | 0.015 | 1.0 | 0.34 | 300 | 775 |
| 5A06 | 27 | 265 | 426 | 0.015 | 1.0 | 0.34 | 300 | 864 |
| ZL102 | 20 | 265 | 426 | 0.015 | 1.0 | 0.34 | 300 | 700 |

Table 2: Parameters of Mie-Grüneisen equation of state[Walsh, Rice, McQueen, and Yarger (1957); Johnson and Cook (1983); Lin, Lin, and Zhao (2006); Ma (2008)]

| Material | ρ (g/cm ³) | c_0 (m/s) | S | C_v (J/Kg/K) | Γ |
|----------|-----------------------------|-------------|-------|----------------|----------|
| Al2024 | 2.785 | 5328 | 1.338 | 875 | 2.0 |
| 2A12 | 2.77 | 5328 | 1.338 | 921 | 2.0 |
| 5A06 | 2.64 | 5328 | 1.338 | 921 | 2.0 |
| ZL102 | 2.65 | 5328 | 1.338 | 838 | 2.0 |

is shown in Figure 2 and its discrete model is shown in figure 3. The first bumper is made of aluminum alloy 2A12 with thickness of 10mm, while the second bumper is made of aluminum foam with thickness of 10 mm, which is placed between the spacecraft wall and the first bumper. The base material of the aluminum foam is ZL102, and its relative density is 27%. The wall is made of aluminum alloy 5A06 with thickness of 2 mm. The whole length of the filling Whipple shield structure is 152 mm and the second bumper lies in the middle of it. the distance between two adjacent particles is 0.2 mm .

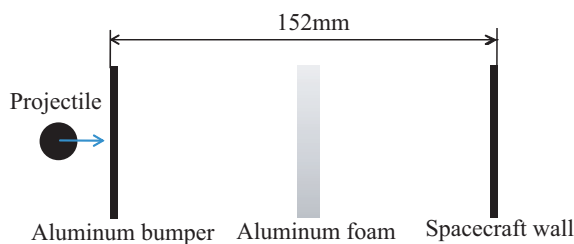


Figure 2: Configuration of the filling Whipple shield structure

The projectile is a sphere with diameter of 6.35 mm and made of aluminum alloy Al2017. Because the mechanical properties of Al2017 are rather close to those of Al2024, the material parameters of Al2024 are used instead in the simulation [Beisel, Gerlach, and Johnson (2006); Hayhurst and Livingstone (1998); Ma (2008)].



Figure 3: MPM simulation model of the filling Whipple shield structure

Three different cases with impact velocities of 2190 m/s , 3410 m/s and 4060 m/s are studied. The projectile impacts normally onto the bumper plate.

Figures 4, 5 and 6 compare the deformation of the first bumper, the second bumper and the spacecraft wall after impact obtained by the experiment [Ma (2008)] and MPM3D, for different impact velocities. Good agreement between the numerical results and experimental results can be observed. In each figure, the pictures shown in the upper part are given by the experiments, and those shown in the lower part are obtained by MPM3D.

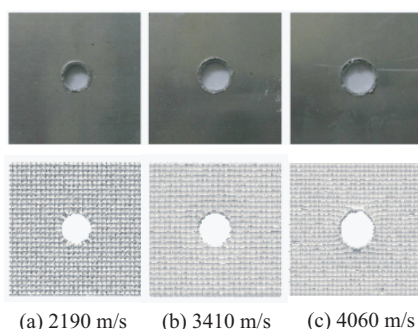


Figure 4: The first bumper after impact. The pictures in the upper part are experimental results[Ma (2008)], while those in the lower part are numerical results.

The shape of the punch hole is irregular due to the randomly sized and distributed holes in the aluminum foam. The diameters of the punch holes in the first bumper, the second bumper and the spacecraft wall obtained by MPM are compared with those given by the experiment [Ma (2008)] in Table 3. The diameter is measured as the diameter of a circle of the same area. Figures 4 and 5 shows that the shape of the punch holes obtained by MPM3D agrees well with that given by the experiment. The maximum error of the punch hole diameter of the first bumper is 1.01% in all three cases, and the maximum error of the punch hole diameter of the second

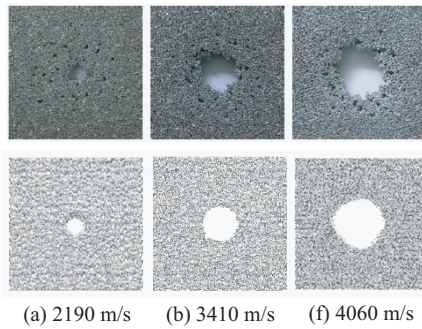


Figure 5: The second bumper after impact. The pictures in the upper part are experimental results[Ma (2008)], while those in the lower part are numerical results.

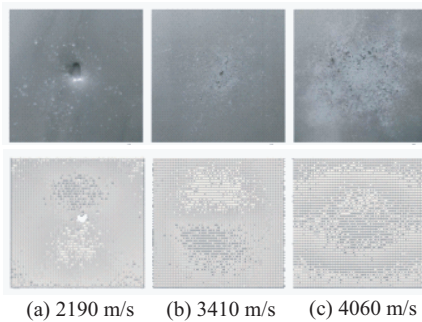


Figure 6: The spacecraft wall after impact. The pictures in the upper part are experimental results[Ma (2008)], while those in the lower part are numerical results.

bumper is 10.07%.

The diameters of punch holes in the first and second bumpers both increase as the projectile velocity increases. The damage of spacecraft wall is minimized when the velocity is 3410 m/s, which means that the inflexion of the ballistic limit curve of the shield occurs near this velocity. It is also noted that the error of the punch hole diameter of the second bumper is larger, because the mechanical properties of the base material are changed a little after machining. On the other hand, a small amount of gas is filled in the internal holes of the aluminum foam, but they are treated as vacuum in the simulations. This may cause some uncertainty[Gibson and Ashby (1997)].

Table 3: The diameters of the punch holes (mm) in the filling Whipple shield structure

| | Impact velocity(m/s) | Experiment | MPM | error |
|---------------------|----------------------|------------|----------|--------|
| The first bumper | 2190 | 9.26 | 9.33 | 0.76% |
| | 3410 | 10.84 | 10.95 | 1.01% |
| | 4060 | 11.48 | 11.50 | 0.17% |
| The second bumper | 2190 | 12.81 | 14.10 | 10.07% |
| | 3410 | 29.72 | 32.16 | 8.21% |
| | 4060 | 38.87 | 41.26 | 6.15% |
| The spacecraft wall | 2190 | 9.46 | 9.57 | 1.16% |
| | 3410 | No bulge | No bulge | - |
| | 4060 | Bulge | Bulge | - |

5.2 Sandwich Whipple shield structure

To investigate the protection capacity of different shield structures against the debris impact, the sandwich Whipple shield structure subject to the hypervelocity impact of a projectile is studied next. The schematic diagram of configuration of the sandwich Whipple shield structure is shown in Figure 7 and its discrete model is shown in Figure 8. The spherical projectile is made of Al2017 with diameter of 6.35 mm. The projectile impacts normally onto the bumper plate at velocities of 2220 m/s, 3190 m/s and 4170 m/s, respectively. The bumper has a sandwich structure consisting of a 10 mm thick aluminum foam covered by two layers of aluminum alloy 2A12 with thickness of 1 mm each. The base material of the aluminum foam is ZL102, and its relative density is 27%. The spacecraft wall is made of aluminum alloy 5A06 with thickness of 2mm. The whole length of the sandwich Whipple shield structure and the distance between two adjacent particles are the same as the filling one.

Figure 9 compares the damage of the spacecraft wall after impact at different velocities obtained by MPM and those given by the experiment. When the projectile

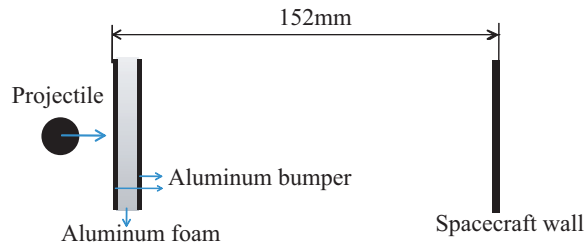


Figure 7: Configuration of the sandwich Whipple shield structure

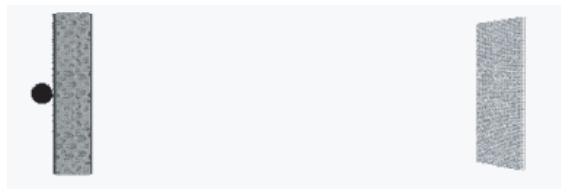


Figure 8: MPM simulation model of the sandwich Whipple shield structure

velocity is 2220 m/s, both the experimental and simulation results are in the critical punched state. Two punch holes are observed both in the experimental and simulation results when the projectile velocity is 3190 m/s. When the projectile velocity is 4170m/s, the experimental result shows 5 punch holes and the simulation result shows 6 punch holes.

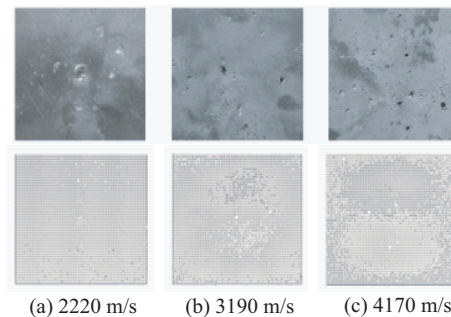


Figure 9: Damage of the spacecraft wall after impact. The pictures in the upper part are experimental results[Ma (2008)], while those in the lower part are numerical results

Based on the numerical results obtained for the filling and sandwich Whipple shield structures, one can conclude that the sandwich protection structure shows better

protection capacity than the filling protection structure for lower velocity (around 2000 m/s) impact. But for higher velocity (around 3000 or 4000 m/s) impact, the filling protection structure is better. This result agrees with the SPH result Ma (2008). The fragments can be efficiently resisted if the protection mass is gathered together under the hypervelocity impact. As the projectile velocity increases, the fragments of the projectile increases, even causing liquefaction or gasification. Then a large number of fragments can be created after the impact. In this case, the filling protection structure will efficiently absorb and disperse the impact energy. Besides, the good agreement between the experimental and simulation results shows that the three-dimensional material point method can effectively solve the hypervelocity impact problems of the aluminum foam.

6 Conclusions

Aluminum foam is an ideal material to absorb impact energy, efficiently resisting the cloud of fragments after hypervelocity impact. In this paper, two different Whipple protection structures of aluminum foam are numerically investigated using our three-dimensional material point method code MPM3D, and numerical results agree well with experimental results. The aluminum foam model is built based on the micro CT scanning images, which can better describe the dynamic behavior of the aluminum foam subject to the debris impact than other macroscopic models because it takes the microstructure of the aluminum foam into account.

It is shown that the material point method has some advantages over FEM in modeling complicated three-dimensional problems based on the micro CT scanned images. The simulation result also shows that the sandwich protection structure has better protection capacity than the filling protection structure when the projectile velocity is low (around 2000 m/s). When the projectile velocity is high (greater than 3000 m/s), the filling protection structure is better. It agrees with the experimental observation.

Acknowledgement: This work was supported by the National Basic Research Program of China (2010CB832701) and National Natural Science Foundation of China (Grant No. 11102097).

References

Ashby, M. F.; Evans, A. G.; Fleck, N. A.; Gibson, L. J.; Hutchinson, J. W.; Wadley, H. N. G. (2006): *Metal Foams: A Design Guide*. Metallurgical Industry Press.

Bardenhagen, S. G. (2002): Energy conservation error in the material point method for solid mechanics. *Journal of Computational Physics*, vol. 180(1), pp. 383–403.

Bardenhagen, S. G.; Kober, E. M. (2000): The generalized interpolation material point method. *Computer Modeling in Engineering and Sciences*, vol. 1(1), pp. 11–29.

Bart-Smith, H.; Bastawros, A. F.; Mumm, D. R.; Evans, A. G.; Sypeck, D. J.; Wadley, H. N. G. (1998): Compressive deformation and yielding mechanisms in cellular al alloys determined using x-ray tomography and surface strain mapping. *Acta Mater*, vol. 46(10), pp. 3583–3592.

Baumeister, J.; Banhart, J.; Weber, M. (1997): Aluminium foams for transport industry. *Materials and Design*, vol. 18(4/6), pp. 217–220.

Beissel, S. R.; Gerlach, C. A.; Johnson, G. R. (2006): Hypervelocity impact computations with finite elements and meshfree particles. *International Journal of Impact Engineering*, vol. 33, pp. 80–90.

Brackbill, J. U.; Kothe, D. B.; Ruppel, H. M. (1988): Flip: a low-dissipation, particle-in-cell method for fluid flow. *Computer Physics Communications*, vol. 48, pp. 25–38.

Carlo, F. D.; Xiao, X.; Tieman, B. (2006): X-ray tomography system, automation and remote access at beamline 2-bm of the advanced photon source. *Developments in X-Ray Tomography V, Proceedings of the SPIE*, vol. 6318, pp. 1605?C7422.

Chen, C.; Lu, T. J. (2000): A phenomenological framework of constitutive modeling for incompressible and compressible elasto-plastic solids. *International Journal of Solids and Structures*, vol. 37(52), pp. 7769–7786.

Christiansen, E. L.; Crew, J. L.; Kerr, J. H. (1996): Hypervelocity impact testing above 10km/s of advanced orbital debris shields. *Shock Compression of Condensed Matter*, vol. 370, pp. 1183–1186.

Christiansen, E. L.; Kerr, J. H. (1993): Mesh double-bumper shield: A low-weight alternative for spacecraft meteoroid and orbital debris protection. *International Journal of Impact Engineering*, vol. 14, pp. 169–180.

Cour-Palais, B. G.; Crew, J. L. (1990): A multi-shock concept for spacecraft shielding. *International Journal of Impact Engineering*, vol. 10, pp. 135–146.

Czekanski, A.; Attia, M. S.; Meguid, S. A.; Elbestawi, M. A. (2005): On the use of a new cell to model geometric asymmetry of metallic foams. *Finite Elements in Analysis and Design*, vol. 41, pp. 1327–1340.

- Daphalapurkar, N. P.; Hanan, J. C.; Phelps, N. B.; Bale, H.; Lu, H.** (2008): Tomography and simulation of microstructure evolution of a closed-cell polymer foam in compression. *Mechanics of Advanced Materials and Structures*, vol. 15, pp. 594–611.
- Degischer, H. P.; Kriszt, B.** (2005): *Handbook of Cellular Metal*. Chemical Industry Press.
- Demiray, S.; Becker, W.; Hohe, J.** (2007): Numerical determination of initial and subsequent yield surfaces of open-celled model foams. *International Journal of Solids and Structures*, vol. 44, pp. 2093–2108.
- Deshpande, V. S.; Fleck, N. A.** (2000): Isotropic constitutive models for metallic foams. *Journal of the Mechanics and Physics of Solids*, vol. 48(6-7), pp. 1253–1283.
- Gama, B. A.; Bogetti, T. A.; Fink, B. K.; Yu, C. J.; Claar, T. D.; Eifert, H. H.; Gillespie, J. W.** (2001): Aluminum foam integral armor: A new dimension in armor design. *composite structure*, vol. 52(3-4), pp. 381–395.
- Gan, Y.; Chen, Z.; Montgomery-Smith, S.** (2011): Improved material point method for simulating the zona failure response in piezo-assisted intracytoplasmic sperm injection. *CMES: Computer Modeling in Engineering & Sciences*, vol. 73(1), pp. 45–75.
- Gibson, L. J.; Ashby, M. F.** (1997): *Cellular Solids, Structure and Properties*. Cambridge University Press.
- Gibson, L. J.; Ashby, M. F.; Zhang, J.; Triantafillou, T. C.** (1989): Failure surfaces for cellular materials under multi-axial loads-(i) modeling. *International Journal of Mechanical Sciences*, vol. 31(9), pp. 635–663.
- Goldman, L. M.** (2007): Principles of ct and ct technology. *Journal of Nuclear Medicine Technology*, vol. 35, pp. 115–128.
- Grenested, J. L.; Bassinet, F.** (2000): Influence of cell wall thickness variations on elastic stiffness of closed-cell cellular solids. *International Journal of Mechanical Sciences*, vol. 42, pp. 1327–1338.
- Gu, Y. T.; Liu, G. R.** (2001): A meshless local petrov-galerkin (mlpg) formulation for static and free vibration analyses of thin plates. *CMES: Computer Modeling in Engineering & Sciences*, vol. 2(4), pp. 463–476.
- Gu, Y. T.; Zhang, L. C.** (2008): Coupling of the meshfree and finite element methods for determination of the crack tip fields. *Engineering Fracture Mechanics*, vol. 75, pp. 986–1004.

Hallquist, J. O. (2006): *LS-DYNA theory manual*. Livermore Software Technology Corporation, 7374 Las Positas Road. Livermore, California 94551, isbn 0-9778540-0-0 edition, 2006.

Hayhurst, C. J.; Livingstone, I. H. (1998): Advanced numerical simulations for hypervelocity impacts - autodyn simulations. Technical Report Report R098, Century Dynamics Ltd., 1998.

Hu, S. S.; Liu, J. F.; Wang, Z. D.; Song, B. (1999): Cushioning and damping of vibration of low density porous material. *Journal of Vibration and Shock*, vol. 18(2), pp. 39–44.

Johnson, G. R.; Cook, W. H. (1983): A constitutive model and data for materials subjected to large strains, high strain rates and high temperatures. In *Proceedings of the 7th International Symposium*.

Li, S.; Liu, W. K. (2002): Meshfree and particle methods and their applications. *Applied Mechanics Reviews*, vol. 55(1), pp. 1–34.

Lian, Y. P.; Zhang, X.; Liu, Y. (2011): Coupling of finite element method with material point method by local multi-mesh contact method. *Computer Methods in Applied Mechanics and Engineering*, vol. 200, pp. 3482–3494.

Lin, G.; Lin, H. G.; Zhao, Y. T. (2006): *Handbook of aluminum alloy*. Machine Press.

Liu, X.; Liu, G. R. (2005): Radial point interpolation collocation method for the solution of nonlinear poisson problems. *Computational Mechanics*, vol. 36(4), pp. 298–306.

Ma, J.; Lu, H.; Wang, B.; Hornung, R.; Wissink, A.; Komanduri, R. (2006): Multiscale simulations using generalized interpolation material point (gimp) method and molecular dynamics (md). *Computer Modeling in Engineering and Sciences*, vol. 14(2), pp. 101–118.

Ma, J.; Lu, H.; Wang, B.; Roy, S.; Hornung, R.; Wissink, A.; Komanduri, R. (2005): Multiscale simulations using generalized interpolation material point (gimp) method and samrai parallel processing. *Computer Modeling in Engineering and Sciences*, vol. 8(2), pp. 135–152.

Ma, S.; Zhang, X.; Lian, Y. P.; Zhou, X. (2009): Simulation of high explosive explosion using adaptive material point method. *CMES: Computer Modeling in Engineering & Sciences*, vol. 39, pp. 101–123.

Ma, S.; Zhang, X.; Qiu, X. M. (2009): Comparison study of mpm and sph in modeling hypervelocity impact problems. *International Journal of Impact Engineering*, vol. 36, pp. 272–282.

- Ma, Z. T.** (2008): *Smoothed particle hydrodynamics method and behavior of space debris protection shields with aluminum foam under hypervelocity impact.* PhD thesis, Harbin Institute of Technology, 2008.
- Ma, Z. T.; Jia, B.; Pang, B. J.** (2007): Behavior of aluminum foams under hypervelocity impact: Validation of numerical simulation. *Advanced Engineering Materials*, vol. 9(10), pp. 888–891.
- Ma, Z. T.; Zhang, X.; Huang, P.** (2010): An object-oriented mpm framework for simulation of large deformation and contact of numerous grains. *CMES: Computer Modeling in Engineering & Sciences*, vol. 55, pp. 61–88.
- Maclay, T. D.** (1993): Topographically modified bumper concepts for spacecraft shielding. *International Journal of Impact Engineering*, vol. 14, pp. 479–489.
- Olsen, G. D.; Nolen, A. M.** (1993): Advanced shield design for space station freedom. *International Journal of Impact Engineering*, vol. 14, pp. 541–550.
- Rabczuk, T.; Eibl, J.** (2006): Modelling dynamic failure of concrete with mesh-free methods. *International Journal of Impact Engineering*, vol. 32(11), pp. 1878–1897.
- Schonberg, W. P.** (1990): Spacecraft wall design for increased protection against penetrations by space debris impact. *American Institute of Aeronautics and Astronautics (AIAA)*, vol. 3, pp. 90–3663.
- Schreyer, H. L.; Zuo, Q. H.; Maji, A. K.** (1994): Anisotropic plasticity model for foams and honeycombs. *Journal of Engineering Mechanics*, vol. 120(9), pp. 1913–1930.
- Shiraki, K.; Terada, F.** (1997): Space station jem design implementation and testing for orbital debris protection. *International Journal of Impact Engineering*, vol. 20, pp. 723–732.
- Sulsky, D.; Chen, Z.; Schreyer, H. L.** (1994): A particle method for history-dependent materials. *Computer Methods in Applied Mechanics and Engineering*, vol. 118(1-2), pp. 179–196.
- Walsh, J. M.; Rice, M. H.; McQueen, R. G.; Yarger, F. L.** (1957): Shock-wave compression of twenty-seven metals, equation of state of metals. *Physical Review*, vol. 108(2), pp. 196–216.
- Whipple, F. L.** (1947): Meteorites and space travel. *Astronomical Journal*, vol. 52, pp. 132–137.
- Zhang, Y. T.; Zhang, X.; Liu, Y.** (2010): An alternated grid updating parallel algorithm for material point method using openmp. *CMES: Computer Modeling in Engineering & Sciences*, vol. 69, pp. 143–165.

CMES: Computer Modeling in Engineering & Sciences

ISSN : 1526-1492 (Print); 1526-1506 (Online)

Journal website:

<http://www.techscience.com/cmес/>

Manuscript submission

<http://submission.techscience.com>

Published by

Tech Science Press

5805 State Bridge Rd, Suite G108

Duluth, GA 30097-8220, USA

Phone (+1) 678-392-3292

Fax (+1) 678-922-2259

Email: sale@techscience.com

Website: <http://www.techscience.com>

Subscription: <http://order.techscience.com>

CMES is Indexed & Abstracted in

Applied Mechanics Reviews; Cambridge Scientific Abstracts (Aerospace and High Technology; Materials Sciences & Engineering; and Computer & Information Systems Abstracts Database); CompuMath Citation Index; Current Contents: Engineering, Computing & Technology; Engineering Index (Compendex); INSPEC Databases; Mathematical Reviews; MathSci Net; Mechanics; Science Alert; Science Citation Index; Science Navigator; Zentralblatt fur Mathematik.